Soft Matter

PAPER

View Article Online
View Journal | View Issue

Cite this: *Soft Matter*, 2025, 21, 6984

Received 20th May 2025,
Accepted 14th August 2025

DOI: 10.1039/d5sm00522a

rsc.li/soft-matter-journal

From single microgels to dense microgel monolayers – investigation by atomic force microscopy

Simon Schog,[a] M. Friederike Schulte,[b] Steffen Bochenek,[a] Timon Kratzenberg[a] and Walter Richtering*[ac]

Due to their unique properties, microgels have garnered large interest in recent times for various applications, including interfacial applications. In this work, we study the internal structure of microgels within microgel monolayers at solid–liquid interfaces using atomic force microscopy (AFM). To capture the rich phase behavior of microgels, the monolayers were deposited at different surface pressures, offering insights into their structural responses under varying compression conditions. The results of the measurements show that the confinement of microgels within a dense monolayer impacts their internal structure and leads to an increase in the contact stiffness, and therefore polymer density, from the third compression regime onward. Additionally, the compression of microgels at the solid–liquid interface leads to the emergence of an attractive interaction between microgels and the sharp AFM tip, resulting in jumps-to-contact in the recorded force–distance curves. The occurrence of jumps-to-contact at high lateral compressions suggests a structural transition within the microgel monolayer, leading to an increase in van-der-Waals and/or electrostatic interactions between microgel and AFM tip.

1 Introduction

Microgels are three-dimensionally crosslinked polymers with a unique combination of properties. They can be synthesized in a variety of shapes, sizes and morphologies[1–3] and are usually spherical objects with sizes from tens of nanometers to tens of micrometers.[4] In response to changes in their local environment, microgels can adapt their swelling behavior and reversibly transition between a swollen and collapsed state with different physicochemical properties.[4,5] This process is most often caused by changes in temperature,[6,7] stemming from the thermoresponsive nature of the commonly used poly-*N*-isopropylacrylamide (PNIPAM). Possible other stimuli include changes in, *e.g.*, pH,[4,8] ionic strength,[8] or solvent composition.[9] The unique combination of properties of macromolecules, hard colloids, and surfactants,[5] as well as the ability to switch the properties on demand has made them interesting candidates for a variety of applications. These include, *e.g.*, the use in catalysis,[10] drug-delivery systems,[11,12] emulsion or foam stabilization,[13–15] tissue engineering,[16,17] or as coatings[18–20] or membranes.[21]

Microgels made with the monomer (NIPAM) and the crosslinker *N*,*N*′-methylenebisacrylamide (BIS) have a heterogeneous internal structure. Due to the kinetics of the radical polymerization, the crosslinker BIS reacts faster than the monomer NIPAM.[22,23] As a result, the crosslinker density of microgels is highest in the center and decreases towards the outside of the microgels. Microgels in the swollen state are often described as a fuzzy sphere[23] with a surface of dangling polymer chains, whereas microgels in the collapsed state resemble homogeneous spheres with a box-like density profile. Like surfactants, microgels readily adsorb to interfaces and maintain their stimuli-responsive swelling behavior.[24–26] The interfacial activity of conventional microgels arises, apart from their chemical composition, from their inhomogeneous structure. The loose polymer strands on the outside of microgels can deform along interfaces and thereby reduce the interfacial free energy. This deformation is counterbalanced by the network elasticity of the microgels and leads to a core–corona or ‘‘fried-egg’’ structure of microgels at interfaces.

Compression isotherms,[24,25,27,28] recorded in Langmuir–Blodgett troughs, show that microgels possess a rich phase behavior at liquid interfaces and can assume (up to) five distinct phase regimes with increasing compression of the interface: (I) a dilute, gaseous stage of single microgels not in

---

[a] *Institute of Physical Chemistry, RWTH Aachen University, 52074 Aachen, European Union, Germany. E-mail: wrichtering@pc.rwth-aachen.de*

[b] *Institute of Physical Chemistry, University of Münster, 48148 Münster, European Union, Germany*

[c] *DWI Leibniz-Institute for Interactive Materials, 52074 Aachen, European Union, Germany*

contact with each other, (II) a hexagonal phase of microgels in corona–corona contact, (III) an isostructural phase transition from corona–corona to core–core contact, (IV) a hexagonal phase of microgels in core–core contact, and (V) the failure of the monolayer.[24,28,29] These five regimes can be observed for microgels in the swollen state; in the collapsed state, the fourth regime of core–core–contact (and compression) is missing as the microgel cores are already collapsed and cannot be compressed further.[24] The existence of the isostructural phase transition was brought into question by recent studies. Kuk *et al.*[30] could not observe it *in situ* for bigger microgels and deduce it to be a drying artifact. On the other hand, however, Rey *et al.*[31] observed the isostructural phase transition in cryo-SEM measurements at the liquid–liquid interface. While the structure of microgels in bulk is often analyzed using scattering techniques such as SLS, SAXS, or SANS,[7,23,32] the analysis of microgels at interfaces is more challenging. Typically, microgel monolayers are prepared in Langmuir–Blodgett troughs, deposited onto solid substrates, and measured *ex situ* using microscopy techniques such as optical, electron, or atomic force microscopy.[24,26] These measurements yield information about the size of the microgels, the topology of the monolayer, and the interparticle distances but they do not contain information about the internal structure of the microgels. Kyrey *et al.* have used grazing incident SANS measurements to obtain information from the microgels' form factor.[33] While this method provides information about the internal structure of microgels at an interface, the structural information is an average since scattering probes the reciprocal space. Backes *et al.* have studied the nanomechanics and nanorheology of microgels at interfaces and show a decrease of the microgels moduli from the center of the microgels to the periphery.[34] Schulte *et al.* have used stiffness tomography, a special AFM technique, to investigate conventional and ultra-low crosslinked (ULC) microgels at solid–liquid interfaces.[35] *Via* the contact stiffness that can be obtained from these measurements, information about the internal structure of the microgels could be gained. Since AFM measurements probe real space, this structural information is obtained with three-dimensional resolution and individual microgels can be identified and analyzed separately which is a huge advantage over scattering techniques, especially for samples with multiple coexistent phases during the isostructural phase transition.

In this contribution, the effect of the confinement on the internal structure of the microgels within a two-dimensional monolayer at the solid–liquid interface is studied. Using a microgel system with known 2D phase behavior,[24] microgel monolayers at different compressions are produced in a Langmuir–Blodgett trough and deposited onto solid substrates. The monolayers are then analyzed (after rehydration) using atomic force microscopy/stiffness tomography with a sharp AFM tip, which leads to three-dimensional data on the internal structure of microgels in the swollen and collapsed states. This data can resolve single microgels within the monolayer, even in regimes with multiple hexagonal phases.

2 Experimental

2.1 Preparation of substrates

2.1.1 Deposition *via* spincoating. The deposition of single microgels *via* spincoating was performed on glass cover slips (22 mm by 22 mm, Menzel Gläser No. 4, Menzel Gläser). The cover slips were cleaned in isopropanol in an ultrasonic bath twice for 15 m and dried with compressed air. The substrates were cleaned and activated in a plasma oven (Femto plasma system, model 1A base unit type A incl. semi-automatic control, Diener electronic GmbH + Co. KG) or ozone oven (UVC-1014, NanoBioAnalytics) for 15 m. The substrates were used immediately afterwards. 120 μL of a cooled 0.05 wt% microgel solution were spincoated onto the substrates with a speed of 2500 rpm and an acceleration of 500 rpm for 30 s (Laurell WS-650MZ-23NPPB spincoater, Laurel Technologies Corporation).

2.1.2 Langmuir–Blodgett depositions. The depositions were performed in a customized liquid–liquid Langmuir–Blodgett trough (KSV NIMA, Biolin Scientific Oy, Finland) made of poly (oxymethylene)glycol with an area of approximately 402 cm^2. The substrates were prepared as described previously.

Before each deposition, the trough was carefully cleaned using ethanol and Milli-Q water. A clean water–decane interface was prepared and cooled to 20 °C using an external water bath. The cleaned glass substrates were submerged in the aqueous phase before the addition of the decane. Microgels were brought to the interface using a solution made from a 10 mg mL^{-1} stock solution and 15% isopropanol. The isopropanol facilitates the spreading of the drops at the interface and has a negligible concentration in the trough.[24] The surface pressure Π was monitored using a platinum Wilhelmy plate (perimeter = 39.24 mm, KSV NIMA, Biolin Scientific Oy, Finland) suspended from an electronic film balance (KSV NIMA, Biolin Scientific Oy, Finland). For the depositions, the barriers of the Langmuir–Blodgett trough were moved with a speed of 5 mm mm^{-1} until the chosen surface pressure for the deposition was reached. After equilibration, the glass substrate was slowly pulled through the interface with a 45° angle and a speed of 0.3 mm min^{-1}.

2.2 Atomic force microscopy

2.2.1 Tapping mode. The microgel monolayers, obtained from Langmuir–Blodgett depositions, were analyzed in the dry state at the solid–air interface using a Dimension Icon AFM with a closed loop (Veeco Instruments Inc., NanoScope 9.4 software, Bruker Corporation), operated in Tapping Mode with an OTESPA tip (nominal resonance frequency 300 kHz, nominal spring constant 26 Nm^{-1}, nominal tip radius $<$ 7 nm, NanoAndMore GmbH, Germany).

2.2.2 Stiffness tomography. For stiffness tomography measurements, the AFM was operated in the force–volume mode of the PeakForce QNM mode. The substrates were mounted into a custom built liquid cell, freshly cleaned with ethanol, and dried with a bellow. A 55 μm thick polyimide foil was placed under the substrates on the side of the photodiode to reduce interference on the detector. The cell was placed on a heating stage

(Dimension Icon Electrochemistry Chuck, Bruker Corporation) with temperature control (Model 335 Cryogenic Temperature Controller, Lake Shore Cryotronics). Filtered double-distilled water was added to the cell to rehydrate the microgels. The sample was allowed to equilibrate for at least 30 min before any measurement was started.

For all measurements, MSNL-10 probes (tip E, nominal resonance frequency 38 kHz, nominal spring constant 0.1 N m^{-1}, nominal tip radius 2 nm Bruker Corporation) were used. Directly prior to use, the probes were treated with oxygen-plasma (1.7–1.8 mbar, 200 W, PVA TePla Plasma System 100, PVA TePla AG) for 6 min. The cantilevers were calibrated using the thermal noise method.[36] The deflection sensitivities were determined from the slope of single force–distance curves measured on the bare substrate. The process was repeated several times for more accurate results. Then, the cantilevers were withdrawn from the sample by 1000 μm and the thermal noise was measured by the thermal tune of the NanoScope 1.9 software. The cantilevers' spring constant were determined from the recorded power spectra.

After calibration, overview images over larger areas were taken in the PeakForce QNM mode to search for regions of interest. The PeakForce tapping frequency was set to 1 kHz and the force setpoint was set to 800–1000 pN. The PeakForce gain was typically set to values of 10–15. After a region of interest has been identified, a force volume measurement was performed. The measurements were taken over an area of 2 μm by 2 μm with a resolution of 192 curves per line. The force setpoint was set to 5 nN and force–distance curves with a ramp size of 1000 nm were measured with a frequency of 10 Hz.

2.2.3 Data analysis. The force–distance curves were analyzed using custom written Matlab scripts. For a more detailed explanation, see the SI.

Firstly, baseline correction of the curve is performed and the measured height is corrected by the deflection of the cantilever to obtain the tip-sample distance. For each curve, a set of potential contact points are determined based on different properties of the data. The methods for these points include (i) the ratio of variances before and after each point,[37] (ii) a cusum approach,[35] (iii) an exponential fit,[35] and (iv) a minimum determination. The script determines which potential contact point to choose as the correct contact point (see also Fig. S9) and shifts the curve so the contact point is at zero sample-tip separation. The measured height image can be corrected for the additional height information from the force–distance curve to yield the corrected height image.

To visualize the data, a 4D matrix is constructed which contains information about the x, y, and z positions of each contact stiffness, k_N, value. Planes are constructed through the centers of the microgels at different angles which visualize the contact stiffness through color values. For each measurement, multiple slice planes from multiple microgels are averaged to obtain averaged contact stiffness profiles of microgels.

3 Results and discussion

3.1 Single microgels

The microgels used in this study were synthesized by Bochenek *et al.*, as reported in 2019.[24] They are NIPAM-based microgels with approximately 4 mol% BIS as a crosslinker and a volume phase transition temperature of roughly 32 °C in water. In bulk, the microgels have hydrodynamic radii, determined *via* dynamic light scattering, of $R_{\mathrm{h},27\,^{\circ}\mathrm{C}}$ = (144 ± 2) nm in the swollen state and $R_{\mathrm{h},35\,^{\circ}\mathrm{C}}$ = (101 ± 2) nm in the collapsed state (see Fig. S1). The polymer density profiles of the microgels have been studied *via* small angle neutron scattering[24] and show that the swollen microgels can be described as a fuzzy sphere and the collapsed microgels can be described using a box-like density profile (see Fig. S2 and S3).

AFM images of single microgels at the solid–air interface can be seen in Fig. 1(A) and (B). The height image of the microgels (see Fig. 1(A)) depicts hemispherical objects with a height of approx. 20 nm and a diameter of approx. 350 nm which is in agreement with previous findings.[24,38] These dimensions merely reflect the size of the microgels' core; in the dried state at the solid–air interface, the coronae of the microgels are too flatly adsorbed to the substrate to be visualized in the height image. The phase image (see Fig. 1(B)), however, reveals the coronae of the microgels in contrast to the microgels' cores and the substrate and allows the actual dimensions of single microgels (not within corona–corona contact with other microgels) to be determined.

In order to obtain information about the internal structure of the rehydrated microgels at the solid–liquid interface, stiffness tomography measurements were performed.[35] In these measurements, a sharp AFM tip is moved in z towards the

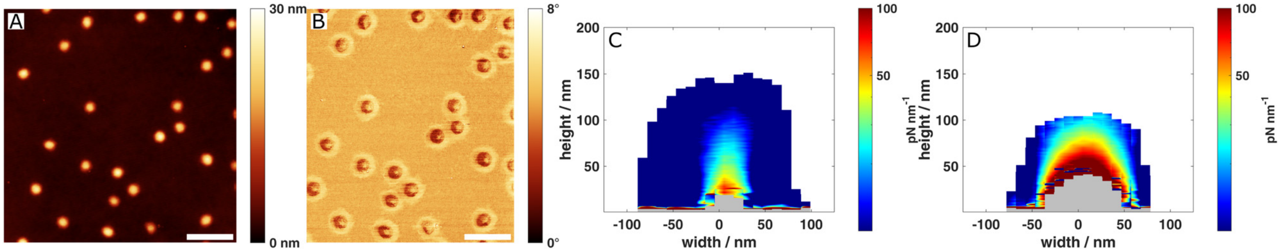

Fig. 1 (A) Height image of single dry microgels at the solid–air interface. (B) Corresponding phase image of single dry microgels at the solid–air interface. (C) Average contact stiffness profile of single rehydrated microgels at the solid–liquid interface at 27 °C. (D) Average contact stiffness profile of single rehydrated microgels at the solid–liquid interface at 35 °C. The scale bars in (A) and (B) are 1 μm long.

sample and the deflection of the cantilever due to sample–tip interactions is continuously monitored. This process is repeated in every pixel of the x–y grid. The resulting force–distance curves in each pixel of the AFM measurement are corrected and their slope, the contact stiffness k, as a function of the x, y, and z position is obtained using a custom written MATLAB app. Representative force–distance curves on the bare glass substrate, the side of a microgel, and the center of a microgel are shown in Fig. S7.

The internal structure of the microgels is depicted in Fig. 1(C) at 27 °C and in Fig. 1(D) at 35 °C. These temperatures are below and above the VPTT of the microgels and therefore depict the microgels in the swollen or the collapsed state, respectively. The figures show averaged contact stiffness profiles of single rehydrated microgels at the solid–liquid interface which were obtained by extracting k along slice planes through multiple microgels at multiple angles and subsequently averaging over all single profiles. The colored regions of the profiles show contact stiffnesses that were obtained from force–distance curves in which the sharp AFM tip penetrated into the microgel networks.[39] Blue areas indicate low contact stiffnesses, correlating with low polymer density, and red areas indicate high contact stiffnesses, correlating with higher polymer density. Regions that are white indicate areas without a contact stiffness, corresponding to the zero force baseline of the force–distance curves. In these regions, the tip does not interact with the sample and therefore, no information can be gained. The gray area in the center of the microgels indicates a region which could not be reached by the sharp AFM tip. As measurements are carried out with a finite threshold force (in this study 5 nN), it is possible that the tip does not penetrate the entire microgel if the microgel is very large or very stiff (or a combination thereof). While the measurements do not provide data within this gray area, the size of the gray area can be indicative of the internal structure of the microgels; that is, the denser the polymeric network of the microgels is, the larger the gray area will be in the profiles. The very flat red areas of high stiffness on the bottom are artifacts caused by the glass substrate underneath. A small amount of smoothing is used in the visualization of the data, which causes the (theoretically) infinite slope of force–distance curves on glass to widen and produce high contact stiffnesses in the first few nanometers above it. They should be ignored in the interpretation of the profiles.

The profile of the swollen microgels in Fig. 1(C) shows that the microgels have an inhomogeneous internal structure. Most of the microgel is very soft with a low contact stiffness and only the core of the microgels has an increased polymer density. These findings are qualitatively in agreement with the findings of Schulte *et al.* that were obtained on a similar type of microgel.[35] The profile also shows that the density of the core has different gradients in the lateral and vertical directions. The microgels are roughly 150 nm high and 180 nm wide. Compared to the hydrodynamic diameter of the microgels ($D_{\mathrm{h},27\,^\circ\mathrm{C}}$ = 280 nm),[24] the height of the microgels is roughly equivalent to 0.55 $D_{\mathrm{h},27\,^\circ\mathrm{C}}$ and the width is roughly 0.65 $D_{\mathrm{h},27\,^\circ\mathrm{C}}$. In the collapsed state, the microgels change in two regards: firstly, they become much smaller, with a height of approx. 110 nm and a width of approx. 160 nm. Compared to $D_{\mathrm{h},35\,^\circ\mathrm{C}}$ = 202 nm,[24] the height and width of the microgels at the interface are roughly 0.55 or 0.8 $D_{\mathrm{h},35\,^\circ\mathrm{C}}$, respectively. Comparing the microgels below and above the VPTT, the ratio between height and D_h stays equal, but the ratio between width and D_h increases. This finding might be caused by the deposition method; since the microgels were deposited in the swollen state below the VPTT, the adhesion between polymer and glass substrate might be so high that the collapse of the microgel network in the lateral direction might be disturbed. Secondly, their internal structure becomes much stiffer, seen by the increase in the area that is colored red and gray. These changes correspond to the behavior of microgels in bulk; in the swollen state, microgels incorporate large amounts of water and become large and soft, while they extrude water from their network in the collapsed state and become smaller and denser. However, the profile shows that there is still a considerable amount of soft polymer network on the periphery of the microgels. Due to experimental reasons (reduction of evaporation over the long measurement windows) and for comparison with previous studies in our group,[35] the higher temperature was chosen as 35 °C which is slightly above the VPTT of the microgels in bulk. As the collapse of microgels is a continuous process, the microgels are not completely collapsed at 35 °C (compare also the DLS data in Fig. S1) and therefore exhibit a surface that is still soft. Measurements on the exact same microgels with a colloidal probe at 40 °C show that the microgels still have a soft surface even at a higher temperature.[40] Furthermore, it is known that pNIPAM microgels in the collapsed state still contain a considerable amount of water.[23]

3.2 Microgel monolayers

We aimed to deposit microgel monolayers in different compression regimes and, therefore, in different 2D phase structures to investigate the influence of the different monolayer structures on the properties of the microgels within the monolayers. Microgel monolayers were obtained from Langmuir–Blodgett depositions.[24] Height images of the dried monolayers were recorded with an AFM in tapping mode (see Fig. 2(A)–(C)) to analyze the 2D phase structure of the monolayers. The three microgel monolayers were deposited at surface pressures Π of 15 mN m^{-1}, 28 mN m^{-1}, and 30.5 mN m^{-1}; therefore, film 1 is in the second compression regime of corona–corona contact, film 2 is at the beginning of the third regime, characterized by the onset of the isostructural phase transition, and film 3 is at the end of the third regime.

The height images show that the obtained monolayers exhibit the intended 2D phase structures. Film 1 (see Fig. 2(A)) shows well-separated microgels with hexagonal packing. Film 2 (Fig. 2(B)) consists of microgels in two different phases; the majority of microgels are in corona–corona contact and form a hexagonal packing of separated microgels, similar to the structure of Film 1. A small amount of microgels has undergone the isostructural phase transition and form small clusters of

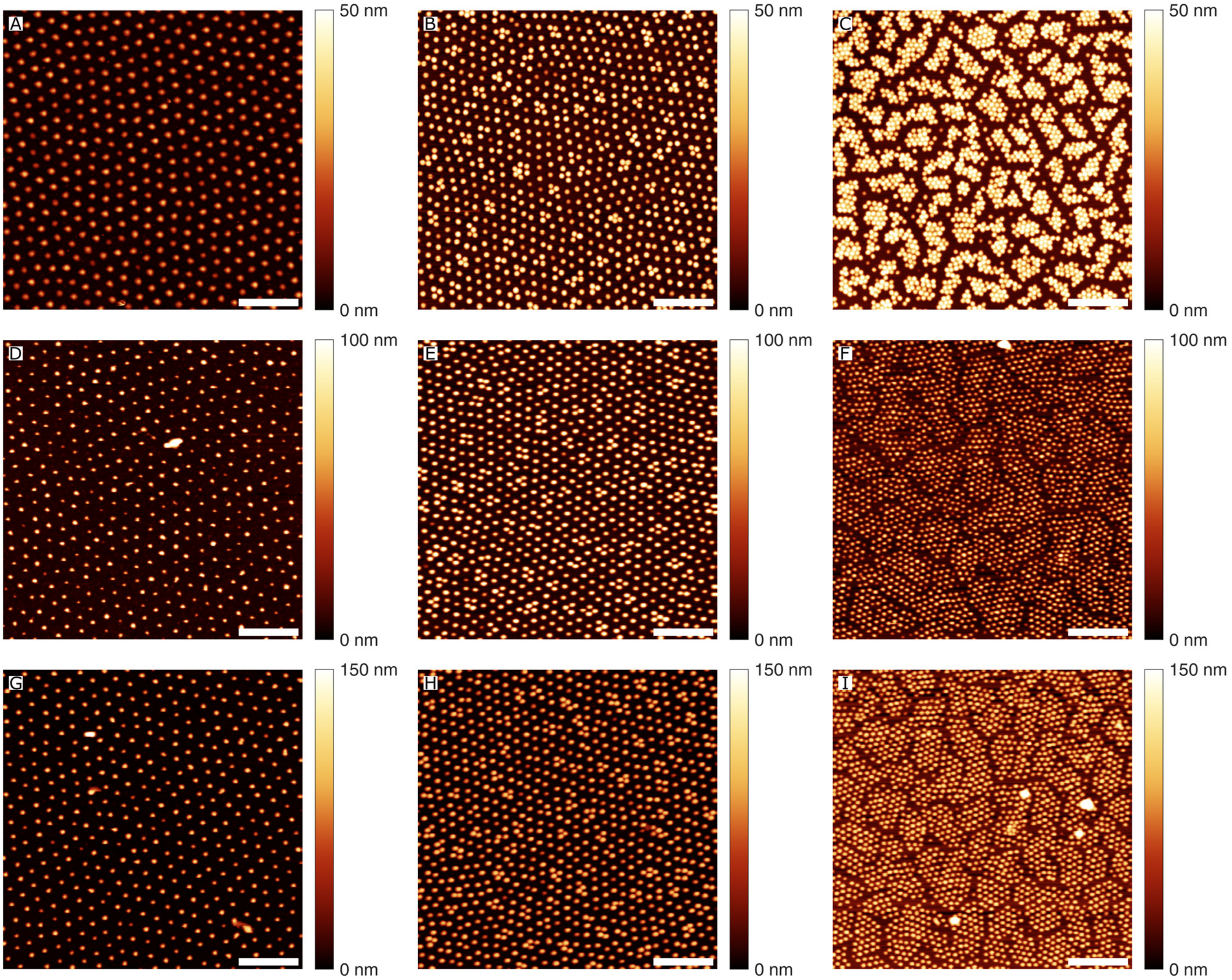

Fig. 2 (A) Height image of dry microgel film 1 (Π = 15 mN m^{-1}) at the solid–air interface. (B) Height image of dry microgel film 2 (Π = 28 mN m^{-1}) at the solid–air interface. (C) Height image of dry microgel film 3 (Π = 30.5 mN m^{-1}) at the solid–air interface. (D) Height image of rehydrated microgel film 1 (Π = 15 mN m^{-1}) at the solid–water interface at 27 °C. (E) Height image of rehydrated microgel film 2 (Π = 28 mN m^{-1}) at the solid–water interface at 27 °C. (F) Height image of rehydrated microgel film 3 (Π = 30.5 mN m^{-1}) at the solid–water interface at 27 °C. (G) Height image of rehydrated microgel film 1 (Π = 15 mN m^{-1}) at the solid–water interface at 35 °C. (H) Height image of rehydrated microgel film 2 (Π = 28 mN m^{-1}) at the solid–water interface at 35 °C. (I) Height image of rehydrated microgel film 3 (Π = 30.5 mN m^{-1}) at the solid–water interface at 35 °C. The scale bars are 2 μm long. Images A–C were recorded in tapping mode and images D–I were recorded in PeakForce Tapping mode.

Table 1 Calculated nearest-neighbor distances of the first and second hexagonal phases, NND_{1st} and NND_{2nd}, for the dried and rehydrated microgel monolayers. Measurements for the rehydrated microgel monolayers were performed at 35 °C

	Π/mN m^{-1}	$\text{NND}_{\text{1st,dry}}$/nm	$\text{NND}_{\text{2nd,dry}}$/nm	$\text{NND}_{\text{1st,rehyd}}$/nm	$\text{NND}_{\text{2nd,rehyd}}$/nm
Film 1	15	503 ± 45	—	503 ± 80	—
Film 2	28	388 ± 55	216 ± 49	369 ± 61	225 ± 50
Film 3	30.5	406 ± 96	169 ± 33	234 ± 61	208 ± 33

roughly 3–7 microgels in core–core contact. In Film 3 (see Fig. 2(C)), the isostructural phase transition is almost complete. The majority of microgels are in clusters with core–core-contact and only a few microgels are separated in corona–corona contact. An increase in the microgels' height can be observed with increasing compression (seen as an increase in the brightness of the microgels in the images).

In preparation of the force–volume measurements at the solid–liquid interface, the monolayers had to be rehydrated and heated to 27 °C or 35 °C. Overview images of the monolayers at the solid–liquid interface were recorded with an AFM in PeakForce Tapping mode (see Fig. 2(D)–(I)) to (a) visualize the film structure and (b) find good positions for the force–volume measurements.

The nearest-neighbor distances (NND) of the monolayers are given in (see Table 1). Each lattice of the microgel monolayer has its own NND; NND_{1st} is the NND of the first (large) lattice of microgels in corona–corona contact and NND_{2nd} is the second (small) lattice of microgels in core–core contact. An analysis of the NNDs shows that the NNDs are mostly unaffected by the rehydration process, as the NNDs of the dry and rehydrated monolayers are similar and within the margin of error of each other. The notable exeption to this finding is film 3, for which $NND_{1st,dry}$ is much larger than $NND_{1st,rehyd}$ and $NND_{2nd,dry}$ is lower than $NND_{2nd,rehyd}$. The difference in the NND_{1st} values can be explained by the low sample size in the measurements. Since only very few microgels are still in the first phase, the nearest neighbor distances can vary strongly between the different images. Due to technical differences between the AFM modes, the images of the rehydrated microgel monolayers were recorded with a lower resolution to reduce the measurement time, which might contribute to the deviations.

The AFM images show that the microgel monolayers persist after rehydration without changing their phase structure. However, the rehydrated monolayers exhibit some protrusions from the monolayer (see Fig. 2(I)). In general, the monolayers are stable at the solid–liquid interface over multiple days; however, sometimes microgels detach from the surface, especially after frequent temperature changes, and might reattach somewhere else on the substrate and form defects.

When comparing the heights of the microgels in the images, one can see that the height of the dry microgels increases with increasing interfacial compression, as has been previously reported.[24] The height of the rehydrated microgels appears to stay constant across the images at the same temperatures. However, due to the AFM mode used to record these images, we do not want to draw any conclusions from the height of the rehydrated microgels. In PeakForce Tapping mode, images are recorded by applying a certain force on the sample. The force was varied between 800 pN and 1 nN in our measurements to achieve good images. Since different forces were used for the different microgel monolayers and microgels are viscoelastic materials, the applied force has an influence on the measured height. This effect can be seen in Fig. 2(D)–(F) in which the microgels at 27 °C are smaller than 100 nm in the images recorded in PeakForce Tapping mode but roughly 150 nm high in the contact stiffness profiles depicted in Fig. 3). Therefore, we use the PeakForce Tapping mode images for their two-dimensional information about the microgel monolayers and use the results of force–volume measurements to extract the height of the microgels.

The averaged contact stiffness profiles of microgels in monolayers are shown in Fig. 3 (see also the height images in Fig. S4 and S5). The profiles in the top row (Fig. 3(A)–(C)) show the contact stiffness profiles of microgels in the swollen state (at 27 °C with increasing interfacial compression from left to right); the profiles of microgels in the collapsed state at 35 °C are depicted in the bottom row (Fig. 3(D)–(F)). Regarding the topography of the monolayers below the VPTT and the single microgels depicted in Fig. 1, all microgels are roughly 150 nm high at their apex, regardless of compression in the lateral dimension. This is in contrast to the results of the dried microgel monolayers and from neutron reflectometry measurements[41,42] which show that microgels expand orthogonally to the fluid interface upon compression of the monolayer. In addition, dried microgel monolayers show an increase

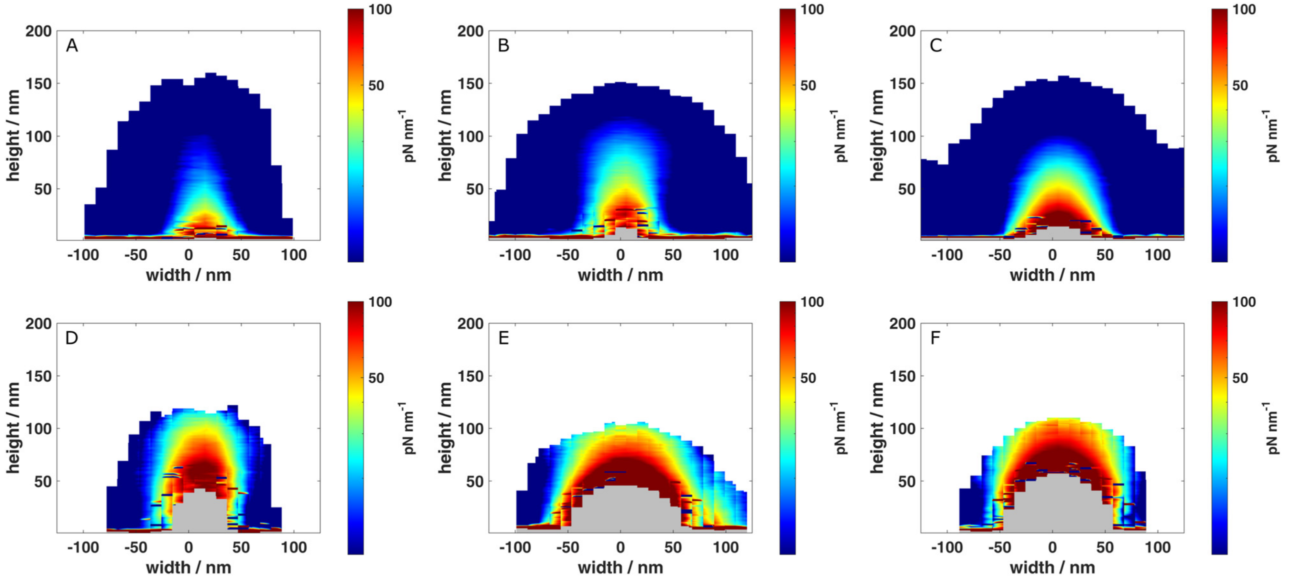

Fig. 3 (A) Average contact stiffness profile of rehydrated microgels in film 1 (Π = 15 mN m^{-1}) at the solid–air interface at 27 °C. (B) Average contact stiffness profile of rehydrated microgels in film 2 (Π = 28 mN m^{-1}) at the solid–air interface at 27 °C. (C) Average contact stiffness profile of rehydrated microgels in film 3 (Π = 30.5 mN m^{-1}) at the solid–air interface at 27 °C. (D) Average contact stiffness profile of rehydrated microgels in film 1 (Π = 15 mN m^{-1}) at the solid–air interface at 35 °C. (E) Average contact stiffness profile of rehydrated microgels in film 2 (Π = 28 mN m^{-1}) at the solid–air interface at 35 °C. (F) Average contact stiffness profile of rehydrated microgels in film 3 (Π = 30.5 mN m^{-1}) at the solid–air interface at 35 °C.

in height with increasing compression after Langmuir–Blodgett deposition to solid substrates[24] which is also observable for the monolayers prepared in this study (see Fig. 2). We attribute these finding at the solid–liquid interface to the adhesion of the polymer to the solid substrate during the deposition and consequent drying of the monolayer. As a consequence, upon rehydration of the microgel for the AFM measurements, the swelling of the microgel network is restricted by the polymer strands adhered to the substrate, leading to a mostly uniform height at the solid–liquid interface.

One can see a slight widening of the microgels from roughly 180 nm for single microgels to roughly 200 nm for microgels in film 1 and 240 nm in film 2. For microgels in film 3, determining the width of a microgel becomes more difficult because the microgels start forming a continuous polymer layer. By using the minima of the profile height as edges, the microgels are roughly 240 nm wide with a gap of roughly 80 nm between apex and minima.

Comparing the widths of the single microgels to microgels within monolayers, the microgels appear to increase in width with increasing compression. We interpret this as a result of the formation of the monolayers. The monolayers are created by depositing microgel onto an oil–water interface and compressing them. By compressing the microgels, polymer at the interface between the microgel cores desorbs and moves into the aqueous subphase (also seen in reflectometry measurements.[42] This leads to an increase in polymer density on the sides of the microgels above the detection-threshold of the AFM and the apparent widening of the microgels in the force–volume measurements.

Overall, the comparison of all films and the single microgels shows that the height stays almost constant while the microgels become slightly wider with increasing compression. The same trend can be seen in the microgel monolayers above the VPTT. The height of 110 nm is the same as the height of single microgels but the microgels become slightly wider (from 160 nm to roughly 180–200 nm).

Regarding the contact stiffness information of the profiles in the swollen state, all monolayers exhibit qualitatively the same structure as the single microgels. Most of the microgels' structure is relatively soft polymer and only the core of the microgels are stiff. However, comparing the microgels in the different stages of compression, one can see an increase in the size (and maximal stiffness) of the core region of the microgels, indicating a change in the microgels internal structure: the microgel network becomes more dense in the core upon compression.

For single microgels and microgels in film 1 at 27 °C, the stiff area (here taken as the green, orange, and red parts) is roughly 75 nm wide at the bottom and reaches a height in the center of roughly 50 nm, roughly a third of the total height. For film 2, the stiff area is also roughly 75 nm wide at the bottom but extend to heights of roughly 80 nm. For film 3, the stiff area is roughly 100 nm wide and roughly 70 nm high. For films 2 and 3, the stiff core reaches half the height of the microgels and the very stiff red regions of the microgels extend vertically as high as the entire stiff region of single microgels and microgels in film 1. Thus, the effect only appears upon compression beyond regime II (hexagonal packing of microgels in corona–corona contact) as the stiffness of the microgels in film 1 is almost identical to single microgels.

The densification of the microgel network is also discernible in the collapsed state of the microgels. At 35 °C, the stiff region of single microgels and microgels in film 1 are approx. 100 nm and 90 nm wide and extend the full height of the microgels, reaching 100 nm and 110 nm in height. For films 2 and 3, the stiff regions are roughly 120 nm wide, although the artifacts from averaging makes the determination of the end of the stiff regions on the sides difficult. Both stiff regions reach heights of 110 nm.

Besides the spatial extend of the stiff regions, the profiles also differ in the actual stiffnesses. Whereas the profiles of single microgels and microgels in film 1 end with a cyan to dark-blue color at the apex, the profile of the microgels in film 2 and 3 end in a yellow to cyan color or a light red color, respectively. The increase in contact stiffness is also visible in the lateral direction, since the dark blue region of low contact stiffness decreases with increasing compression. The increase in stiffness is therefore observable in the center of the microgels as the increase in the stiff areas and in the periphery of the microgels as the widening of the microgels.

The structures portrayed in Fig. 3 only show the average microgel; averaging contact stiffness profiles across multiple microgels next to each other is difficult due to small deviations in the orientation and distances between them. Fig. 4 shows unaveraged contact stiffness profiles along individual slice planes through all investigated microgel samples (see Fig. S8 for the positions of the slice planes in the AFM measurements). In general, the contact stiffness data in these profiles is in agreement with the averaged microgel structures. Some microgels, however, show lower contact stiffnesses in their center than their neighbors due to the alignment of the microgels in respect to the slice plane and should be disregarded.

More interestingly, the slice planes shows the structure of the monolayers in between microgels. For the measurements at 27 °C, single microgels and microgels in film 1 are all completely seperated from each other. Starting with film 2, the isostructural phase transition causes the microgels to be split into two phases: microgels in the first phase (with higher NNDs) are still seperated from each other, microgels in the second phase (with lower NNDs) are in contact with each other. The microgels in film 3 are all in the second hexagonal phase. The three microgels on the left side are in contact with each other whereas there are small gaps between the microgels on the right. The slice plane is oriented in such a way that the microgel on the very right is on the edge of a cluster and the microgels on the left are inside the cluster. This demonstrates that the clusters of microgels form a continuous polymer coating on the substrate that is only discontinued between the individual clusters and near their edges. It is also worth noting that the microgels near the edge of the cluster are significantly smaller than the microgels on the inside of the cluster. For the

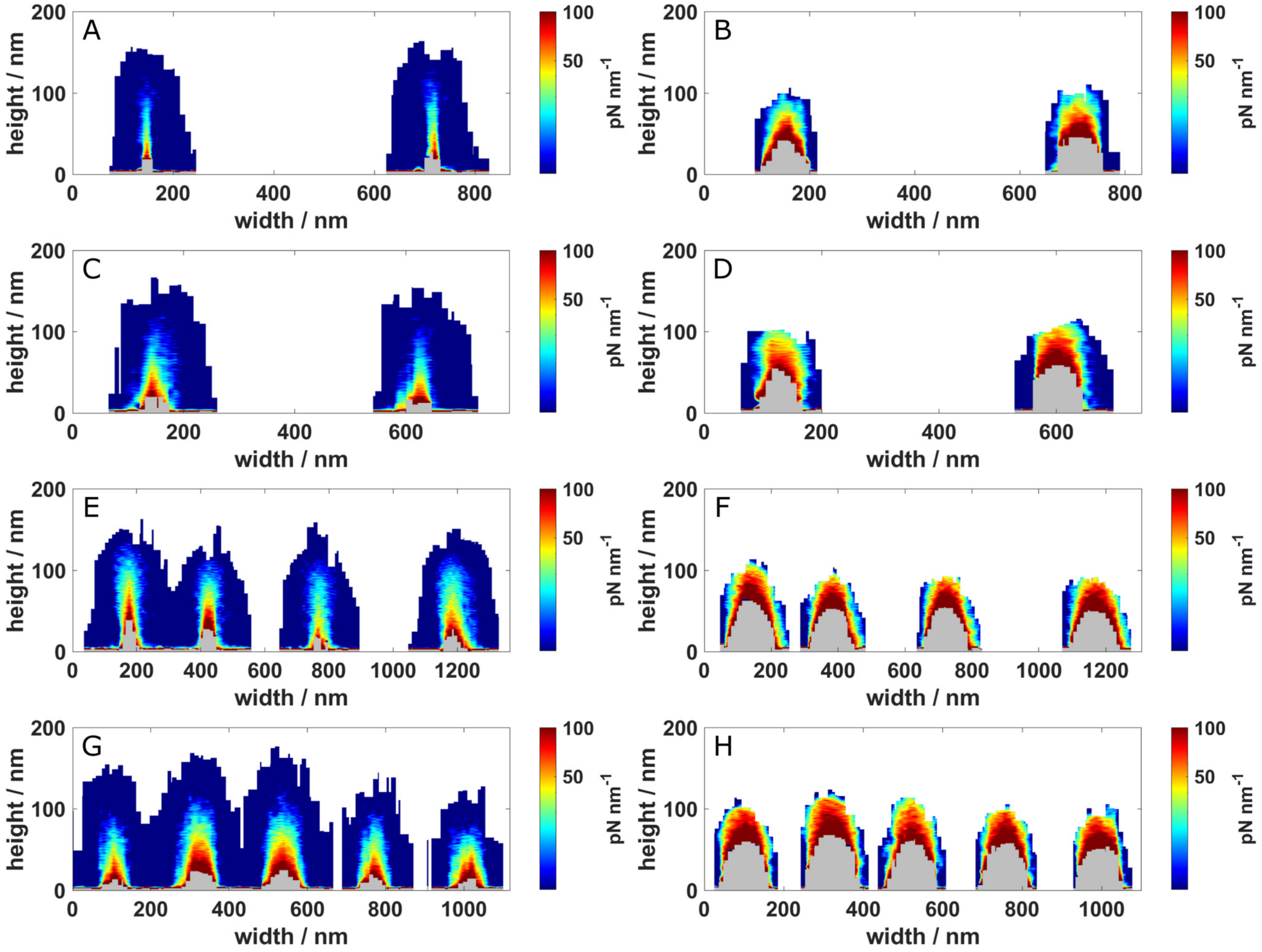

Fig. 4 Individual slice planes through single microgels and microgel monolayers at the solid–liquid interface at 27 °C (A), (C), (E), (G) and 35 °C (B), (D), (F), (H). The planes are taken from single microgels (A), (B), microgels in film 1 (C), (D), microgels in film 2 (E), (F), and microgels in film 3 (G), (H).

measurements at 35 °C, all microgels are separated from each other, regardless of degree of compression of the monolayer or whether the microgels are in the first or second hexagonal phase. The separation of microgels, even in the second phase in "core–core contact", is due to the temperature. The original depositions were performed at 20 °C and lead to dry microgel

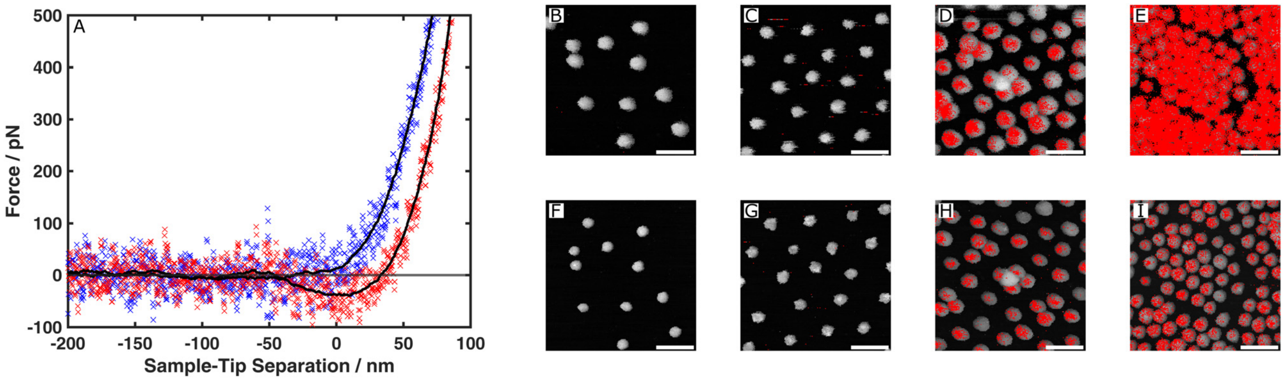

Fig. 5 (A) Excerpts of two force–distance curves to demonstrate the jumps-to-contact. The blue curve is taken from the center of a microgel in the measurement of film 1 at 27 °C. The red curve is taken from the center of a microgel in the measurement of film 3 at 27 °C. (B)–(I) Corrected height images of microgels at the solid–liquid interface at 27 °C (B)–(E) and 35 °C (F)–(I). The corrected height images belong to the measurement of single microgels (B), (F), microgels in film 1 (C), (G), microgels in film 2 (D), (H), and microgels in film 3 (E), (I). Pixels in which the corresponding force–distance curve contains a jump-to-contact are marked in red. The scale bars are 500 nm long.

monolayers with up to two phases, commonly referred to as ''corona–corona contact'' and ''core–core contact'' (see Fig. 2(A)–(C)). Upon rehydration of the monolayers to 27 °C, the microgels in the second phase remain in core–core contact; however, by heating them to 35 °C, the microgels collapse and become smaller. As the microgels are immobilized on a solid substrate, they cannot rearrange and therefore, gaps between the microgels are formed. The terms ''corona–corona contact'' and ''core–core contact'' should be understood as a description of the dry monolayers; for rehydrated monolayers, we continue using these names for consistency, even if the core–core contact is evidently lost in our measurements above the VPTT.

3.3 Interactions between microgels and AFM tip

The evaluation of the individual force–distance curves across all measurements has shown unexpected changes in the interactions between the microgels and the sharp AFM tip, namely the appearance of jumps-to-contact (JTCs) in the curves (see Fig. 5(A) for an example). The position of all jumps-to-contact are marked in red in Fig. 5(B)–(I). No jumps-to-contact are observed for measurements of single microgels both below and above the volume phase transition temperature. This finding is in agreement with previous works from our group on single microgels in which jumps-to-contact have never been observed.[35,39] For film 1, jumps-to-contact can only be observed in a small number of erroneous pixels (almost exclusively on the glass substrate) in the measurements and should be disregarded. For film 2, jumps-to-contact start to appear in the measurements at both temperatures. They are located only in pixels on microgels and make up less than half of all curves measured on microgels. For film 3, force–distance curves with jumps-to-contacts make up almost all curves measured on microgels in the swollen state. In the collapsed state, there are also some jumps-to-contact, but a much smaller amount (comparable to the amount of jumps-to-contact for film 2 in the collapsed state).

The data shows that the occurrence of jumps-to-contact depend on both temperature and the compression of the microgel monolayers. Jumps-to-contact seem to only appear from the third compression regime of microgels onwords and they are more numerous in the swollen state than in the collapsed state. The jumps-to-contact also seem to be positioned more on the left side of the microgels than on their right side.

The occurrence of small jumps-to-contact in the approach curve is a known phenomenon. In a number of studies on poylmer brushes,[43,44] JTC were observed for polymer brushes with low grafting density. In these cases, they were caused by interactions between the AFM tip and the solid substrate beneath the polymer brushes. Higher grafting densities increase steric repulsion and lead to a disappearance of the JTC. JTC can also appear in force–distance curves by collapsing the polymer brushes *via* co-nonsolvency.[45] In the case of polyelectrolyte brushes, JTC can appear and become more pronounced with increasing charge density.[46] In a different study, an increase in salt concentration can increase attractive interactions for polyelectrolyte brushes.[47] The authors also show that a slower approach speed increases the attractive interactions between brushes and a colloidal AFM tip. A different study explains this by the formation and disentanglement of polyelectrolyte complexes.[48] A study on microgels with different crosslinker-to-monomer ratios by Aufderhorst-Roberts *et al.*[49] shows that JTC appear in curves of their most crosslinked microgels. However, the authors only analyzed individual microgels below their VPTT. They discuss that the JTC is possibly caused by stronger van-der-Waals forces caused by a higher polymer concentration near the surface and rule out electrostatic forces.

In the case of our microgel system and AFM experiments, the exact nature of the attractive interactions cannot be extracted from the data. Based on literature on polymer brushes and microgels, there are, however, several possible hypotheses. We can rule out interactions between the tip and the solid glass substrate underneath the microgels as force–distance curves on glass show no attractive interactions. The occurrence of the JTC in the third compression regime and above might be caused by an increase in polymer concentration. This could increase van-der-Waals interactions between microgel and tip. In addition, the dangling polymer chains on the periphery of the microgels might reorientate themselves due to the lateral compression and extend further into the aqueous phase. Upon approach of the AFM probe, the extended polymer chains might adsorb onto the probe and effectively ''pull'' it down towards the microgel.

The JTC might also be caused by electrostatic interactions. Our microgels are slightly positively charged due to the initiator fragments and the comonomer which contains primary amine moieties. The electrophoretic mobility of the microgels increases with increasing temperature due to a reduction in the microgels' size and a redistribution of the positive charges towards the surface of the microgels.[38] The AFM tip is made of silicon and has a slightly negative charge after activation in the plasma/ozone oven. It is therefore feasible that there is an electrostatic attraction between tip and microgels. Adding salt to screen electrostatic interactions is not possible with our microgel system. Our microgels lose colloidal stability in bulk upon addition of even small amounts of salt and at the solid–liquid interface, they detach very easily on contact with the AFM tip which prevents force–volume measurements. Another strategy to check for electrostatic interactions would be changing the microgel system from a slightly positively charged one to a slightly negatively charged one. Changes to the microgel system (which would have to be synthesized first with similar sizes and structures to compare the results and characterized in bulk and at the interface) can necessitate changes to the experimental procedure like functionalization of the substrate and/or AFM tip to produce stable measurements. This time-consuming process is outside the scope of this work and we have therefore opted to present the data that we have and state possible origins/contributions to the interactions that we see in our data.

The apparent differences between the left and right side of the microgels is reminiscent of scan directional effects in AFM images. However, since the AFM records the force–volume images in a zig-zag pattern (by changing the scan direction in each line), the apparent differences are caused by differences in position. The anisotropic distribution can be seen in two data sets (for film 2 and film 3) which were measured at different times with different AFM tips and random orientation of the substrates within the liquid cell. Therefore, we assume the geometry of the AFM is responsible for these results. The AFM tip is always positioned the same way and is (a) angled slightly at the interface and (b) has an asymmetric shape which is steeper on the left side of the tip and flatter on the right side. When the tip measures the left side of a microgel, the microgel interacts more with the flatter side of the tip (and *vice versa*), which might explain the distribution of the jumps-to-contact in two different, randomly orientated monolayers (films 2 and 3) measured with different AFM tips.

4 Conclusions

In this work, we studied the properties of microgels within dense monolayers at the solid–liquid interface. This work shows that microgel monolayers prepared *via* Langmuir–Blodgett deposition persist after rehydration without changes to the crystal lattice. Our measurements show that the confinement of microgels in a monolayer has almost no impact on the height of the microgels and only causes a slight change in width, but has a pronounces effect on the internal structure of microgels. Starting in regime III, the microgels show an increase in contact stiffness, and therefore polymer density, in their cores. Microgels in regime II show contact stiffnesses indistinguishable from single microgels. This densification upon lateral compression is most apparent in the swollen state but also exists in the collapsed state of the microgel.

In addition, the analysis of the individual force–distance curves shows a change in the interactions between the AFM tip and the microgels, namely the appearance of jumps-to-contact at high compressions. While the exact cause of the jumps-to-contacts cannot be directly extracted from our measurements, they are likely related to van-der-Waals forces between the AFM tip and the microgel or electrostatic forces. The emergence of jumps-to-contact show that there are apparent structural changes in the microgel monolayers which cannot be captured with stiffness tomography. However, further experiments are needed to try and discern the exact cause and changes of these attractive interactions.

Overall, our data shows that the properties of microgels at solid–liquid interfaces are dependent on the compression of the monolayer and can differ from results obtained at fluid interfaces. Microgels in the second regime are qualitatively almost identical to single microgels in terms of size and internal structure. Changes in the microgels' internal structure and interactions with the tip only start to appear in regime III at higher compressions. These findings are of particular relevance for a wide field of applications for microgel-covered interfaces such as coatings for cell adhesion or sensor technologies. The knowledge about the three-dimensional structure of microgel films in different compressions and associated "softness" can be crucial for the success of these applications and can be obtained from force spectroscopic measurements on microgels.

Author contributions

S. S.: data curation, formal analysis, investigation, software, visualization, writing – original draft. M. F. S.: conceptualization, methodology, S. B.: conceptualization, methodology, software. T. K.: software. W. R.: conceptualization, funding acquisition, supervision, writing – original draft.

Conflicts of interest

There are no conflicts of interest to declare.

Data availability

Data for this article are available at RADAR4Chem at **https://doi.org/10.22000/0b754r92k72b6ngg**.

Supplementary information available: They include scattering data (DLS and SANS) of the microgels, the height and corrected height images of the force-volume measurements, the phase images of the microgel monolayers, representative force-distance curves, a description of the algorithm to detect the contact point and the results for all measurements, and the position of all individual slice planes within the force-volume measurements. See DOI: **https://doi.org/10.1039/d5sm00522a**.

Acknowledgements

The authors acknowledge financial support of the Deutsche Forschungsgesellschaft (DFG) within project B8 of "SFB 985 – Functional Microgels and Microgel Systems" (Project number 191948804). This work contains data obtained using the KWS-2 instrument operated by Jülich Centre for Neutron Science (JCNS) at the Heinz Maier-Leibnitz Zentrum (MLZ), Garching, Germany. RWTHgpt has been used for minor text revisions.

Notes and references

1 A. C. Nickel, A. Scotti, J. E. Houston, T. Ito, J. Crassous, J. S. Pedersen and W. Richtering, *Nano Lett.*, 2019, **19**, 8161–8170.
2 L. Steinbeck, D. L. Braunmiller, H. J. M. Wolff, V. Huettche, J. Wang, M. Wessling, J. J. Crassous and J. Linkhorst, *Adv. Mater. Technol.*, 2023, 2300044.
3 W. Xu, A. Rudov, A. Oppermann, S. Wypysek, M. Kather, R. Schroeder, W. Richtering, I. I. Potemkin, D. Wöll and A. Pich, *Angew. Chem., Int. Ed.*, 2020, **59**, 1248–1255.
4 F. A. Plamper and W. Richtering, *Acc. Chem. Res.*, 2017, **50**, 131–140.
5 M. Karg, A. Pich, T. Hellweg, T. Hoare, L. A. Lyon, J. J. Crassous, D. Suzuki, R. A. Gumerov, S. Schneider, I. I. Potemkin and W. Richtering, *Langmuir*, 2019, **35**, 6231–6255.

6 R. Pelton and P. Chibante, *Colloids Surf.*, 1986, **20**, 247–256.

7 M. Brugnoni, A. Scotti, A. A. Rudov, A. P. H. Gelissen, T. Caumanns, A. Radulescu, T. Eckert, A. Pich, I. I. Potemkin and W. Richtering, *Macromolecules*, 2018, **51**, 2662–2671.

8 S. K. Wypysek, A. Scotti, M. O. Alziyadi, I. I. Potemkin, A. R. Denton and W. Richtering, *Macromol. Rapid Commun.*, 2020, **41**, 1900422.

9 K. Nothdurft, D. H. Müller, T. Brands, A. Bardow and W. Richtering, *Phys. Chem. Chem. Phys.*, 2019, **21**, 22811–22818.

10 R. Borrmann, V. Palchyk, A. Pich and M. Rueping, *ACS Catal.*, 2018, **8**, 7991–7996.

11 D. Sivakumaran, D. Maitland and T. Hoare, *Biomacromolecules*, 2011, **12**, 4112–4120.

12 M. Dirksen, T. A. Kinder, T. Brändel and T. Hellweg, *Molecules*, 2021, **26**(11), 3181.

13 B. Brugger and W. Richtering, *Langmuir*, 2008, **24**, 7769–7777.

14 M. Destribats, V. Lapeyre, M. Wolfs, E. Sellier, F. Leal-Calderon, V. Ravaine and V. Schmitt, *Soft Matter*, 2011, **7**, 7689.

15 M. Kühnhammer, K. Gräff, E. Loran, O. Soltwedel, O. Löhmann, H. Frielinghaus and R. von Klitzing, *Soft Matter*, 2022, **18**, 9249–9262.

16 D. L. Braunmiller, S. Babu, D. B. Gehlen, M. SeuÃŸ, T. Haraszti, A. Falkenstein, J. Eigen, L. De Laporte and J. J. Crassous, *Adv. Funct. Mater.*, 2022, **32**, 2202430.

17 J. P. Newsom, K. A. Payne and M. D. Krebs, *Acta Biomater.*, 2019, **88**, 32–41.

18 K. Uhlig, T. Wegener, Y. Hertle, J. Bookhold, M. Jaeger, T. Hellweg, A. Fery and C. Duschl, *Polymers*, 2018, **10**(6), 656.

19 S. Schmidt, H. Motschmann, T. Hellweg and R. von Klitzing, *Polymer*, 2008, **49**, 749–756.

20 S. Schmidt, M. Zeiser, T. Hellweg, C. Duschl, A. Fery and H. Möhwald, *Adv. Funct. Mater.*, 2010, **20**, 3235–3243.

21 M. Dirksen, P. Fandrich, L. Goett-Zink, J. Cremer, D. Anselmetti and T. Hellweg, *Langmuir*, 2022, **38**, 638–651.

22 X. Wu, R. H. Pelton, A. E. Hamielec, D. R. Woods and W. McPhee, *Colloid Polym. Sci.*, 1994, **272**, 467–477.

23 M. Stieger, W. Richtering, J. S. Pedersen and P. Lindner, *J. Chem. Phys.*, 2004, **120**, 6197–6206.

24 S. Bochenek, A. Scotti, W. Ogieglo, M. n Fernández-Rodríguez, M. F. Schulte, R. A. Gumerov, N. V. Bushuev, I. I. Potemkin, M. Wessling, L. Isa and W. Richtering, *Langmuir*, 2019, **35**, 16780–16792.

25 K. Geisel, W. Richtering and L. Isa, *Soft Matter*, 2014, **10**, 7968–7976.

26 K. Kuk, V. Abgarjan, L. Gregel, Y. Zhou, V. Carrasco Fadanelli, I. Buttinoni and M. Karg, *Soft Matter*, 2023, **19**, 175–188.

27 M. Rey, M. n Fernández-Rodríguez, M. Steinacher, L. Scheidegger, K. Geisel, W. Richtering, T. M. Squires and L. Isa, *Soft Matter*, 2016, **12**, 3545–3557.

28 L. Scheidegger, M. n Fernández-Rodríguez, K. Geisel, M. Zanini, R. Elnathan, W. Richtering and L. Isa, *Phys. Chem. Chem. Phys.*, 2017, **19**, 8671–8680.

29 M. M. Schmidt, O.-V. Laukkanen, S. Bochenek, W. S. Schier and W. Richtering, *J. Rheol.*, 2024, **68**, 553–570.

30 K. Kuk, V. Abgarjan, L. Gregel, Y. Zhou, V. Carrasco Fadanelli, I. Buttinoni and M. Karg, *Soft Matter*, 2023, **19**, 175–188.

31 M. Rey, J. Kolker, J. A. Richards, I. Malhotra, T. S. Glen, N. Y. D. Li, F. H. J. Laidlaw, D. Renggli, J. Vermant, A. B. Schofield, S. Fujii, H. Lowen and P. S. Clegg, *Nat. Commun.*, 2023, **14**, 6723.

32 I. Varga, T. Gilányi, R. Mészáros, G. Filipcsei and M. Zrínyi, *J. Phys. Chem. B*, 2001, **105**, 9071–9076.

33 T. Kyrey, M. Ganeva, K. Gawlitza, J. Witte, R. von Klitzing, O. Soltwedel, Z. Di, S. Wellert and O. Holderer, *Phys. B*, 2018, **551**, 172–178.

34 S. Backes and R. von Klitzing, *Polymers*, 2018, **10**(9), 978.

35 M. F. Schulte, S. Bochenek, M. Brugnoni, A. Scotti, A. Mourran and W. Richtering, *Angew. Chem., Int. Ed.*, 2021, **60**, 2280–2287.

36 J. te Riet, A. J. Katan, C. Rankl, S. W. Stahl, A. M. van Buul, I. Y. Phang, A. Gomez-Casado, P. Schön, J. W. Gerritsen, A. Cambi, A. E. Rowan, G. J. Vancso, P. Jonkheijm, J. Huskens, T. H. Oosterkamp, H. Gaub, P. Hinterdorfer, C. G. Figdor and S. Speller, *Ultramicroscopy*, 2011, **111**, 1659–1669.

37 N. Gavara, *Sci. Rep.*, 2016, **6**, 21267.

38 S. Bochenek, A. Scotti and W. Richtering, *Soft Matter*, 2021, **17**, 976–988.

39 M. F. Schulte, A. Scotti, A. P. H. Gelissen, W. Richtering and A. Mourran, *Langmuir*, 2018, **34**, 4150–4158.

40 T. Kratzenberg, S. Schog, S. Bochenek, M. F. Schulte and W. Richtering, *Soft Matter*, 2025, **51**, 5255–5267.

41 S. Bochenek, F. Camerin, E. Zaccarelli, A. Maestro, M. M. Schmidt, W. Richtering and A. Scotti, *Nat. Commun.*, 2022, **13**, 3744.

42 Y. Gerelli, F. Camerin, S. Bochenek, M. M. Schmidt, A. Maestro, W. Richtering, E. Zaccarelli and A. Scotti, *Soft Matter*, 2024, **20**, 3653–3665.

43 Y. Zou, N. A. A. Rossi, J. N. Kizhakkedathu and D. E. Brooks, *Macromolecules*, 2009, **42**, 4817–4828.

44 G. Gao, K. Yu, J. Kindrachuk, D. E. Brooks, R. E. W. Hancock and J. N. Kizhakkedathu, *Biomacromolecules*, 2011, **12**, 3715–3727.

45 X. Sui, Q. Chen, M. A. Hempenius and G. J. Vancso, *Small*, 2011, **7**, 1440–1447.

46 T. Pettersson, A. Naderi, R. Makuška and P. M. Claesson, *Langmuir*, 2008, **24**, 3336–3347.

47 A. Drechsler, A. Synytska, P. Uhlmann, M. Stamm and F. Kremer, *Langmuir*, 2012, **28**, 15555–15565.

48 E. Spruijt, M. A. Cohen Stuart and J. van der Gucht, *Macromolecules*, 2010, **43**, 1543–1550.

49 A. Aufderhorst-Roberts, D. Baker, R. J. Foster, O. Cayre, J. Mattsson and S. D. Connell, *Nanoscale*, 2018, **10**, 16050–16061.